AALBORG UNIVERSITY

DENMARK

Precise Inductor Current Ripple Distribution of Three-Level Active Neutral-Point-Clamped Inverter

Pan, Donghua; Chen, Mengxing; Wang, Xiongfei; Wang, Huai; Blaabjerg, Frede; Wang, Wei

Precise Inductor Current Ripple Distribution of Three-Level Active Neutral-Point-Clamped Inverter

Donghua Pan[1], Mengxing Chen[1], Xiongfei Wang[1], Huai Wang[1], Frede Blaabjerg[1], and Wei Wang[2]

[1] Department of Energy Technology, Aalborg University, Denmark

[2] School of Electrical Engineering & Automation, Harbin Institute of Technology, China

Abstract--**In power electronic converters, the inductor current ripple affects the system power loss and should be minimized. This paper studies in detail the output filter inductor current ripple distribution of a three-level active neutral-point-clamped (3L-ANPC) inverter. The peak-to-peak current ripple per line cycle is precisely derived according to the modulation index. Then, the maximum current ripple is identified, and the concept of average current ripple is proposed to quantify the overall ripple level. An optimal operating point with minimum ripple level is found, and it is chosen as the nominal operation condition of the 3L-ANPC inverter. Simulations are performed in a case study to confirm the theoretical expectations.**

Index Terms--**3L-ANPC inverter, inductor current ripple, modulation index, output filter.**

I. INTRODUCTION

Recently, the progress in photovoltaic (PV) panels has raised its system open-circuit voltage from 1000 V to 1500 V [1]–[3]. A higher DC input voltage can lower power losses in DC transmission cables, and it is a trend in future PV inverters [4], [5]. At such a voltage level, the three-level neutral-point-clamped (3L-NPC) topology is the most popular choice due to its low device stress [6]. The original 3L-NPC topology adopts two diodes to clamp the neutral point [7]. While simple, it suffers from the uneven loss and voltage stress distribution among power devices. To overcome this drawback, the three-level active neutral-point-clamped (3L-ANPC) topology is proposed by replacing clamping diodes with active switches [8]–[11].

For a 3L-ANPC inverter, the modulation of the inverter bridge is of prime importance, since it determines the output voltage harmonics and current ripple distribution. As a main factor that affects the system power loss, the inductor current ripple should be precisely analyzed and diminished. Generally, the *maximum current ripple* per line cycle is applied to quantify the overall ripple level [12], [13]. In fact, it is not adequate since the instantaneous current ripple varies significantly at different phase angles [14]. Hence, a full distribution of the instantaneous current ripple over a line cycle is much meaningful.

The current ripple distribution in three-phase two-level inverters has been investigated in [15] and [16]. A more detailed evaluation was presented in [17], which exhibited the relationship between the peak-to-peak current ripple and the modulation index. The current ripple distribution of a 3L-NPC inverter was calculated in [18] and compared

to a two-level inverter in [19], but it was limited to one specific space-vector modulation (SVM) scheme.

Since the carrier-based sinusoidal pulse-width modulation (SPWM) gives the basis for existing modulation schemes, the current ripple distribution based on SPWM needs to be studied at the first priority, which is the motivation of this paper. By carefully defining the phase intervals according to the modulation index, the peak-to-peak current ripple in each phase interval can be figured out. Accordingly, precise ripple distributions per line cycle are obtained for different modulation indexes. Then, the maximum current ripple in a line cycle can be identified. Moreover, the concept of an *average current ripple* is proposed to quantify the overall ripple level. Through a joint evaluation of the maximum ripple and the average ripple in the entire modulation range, an *optimal* operating point with minimum ripple level is found, which is designed as the nominal operation condition of the 3L-ANPC inverter. A case study is presented to verify the theoretical analysis.

II. SPWM MODULATION OF 3L-ANPC INVERTER

Fig. 1(a) shows a three-phase 3L-ANPC PV inverter feeding into the grid. Silicon carbide (SiC) MOSFETs $S_1 - S_6$ and their antiparallel diodes are adopted to form the inverter phase leg. An *LCL* filter is employed at the grid side due to its superior harmonic attenuating ability [20]–[24]. L_1 is the inverter-side inductor, C is the filter capacitor, and L_2 is the grid-side inductor.

In the 3L-ANPC inverter, there are two neutral current paths, which provide alternatives to clamp the neutral point. The neutral current can flow through either the upper path by turning on S_5 and S_2, or the lower path by turning on S_6 and S_3. Particularly, all four inner switches S_5, S_2, S_6, and S_3 can be turned on simultaneously. In this way, the upper path and the lower path form two-paralleled current paths, which can reduce the on-state resistance as well as the conduction loss during the neutral state. This clamping scheme is noted as the "full clamping", which is especially appealing when SiC MOSFETs are used, since they have excellent current sharing capabilities [25].

The SPWM switching patterns for the full clamping scheme are illustrated in Fig. 1(b), where the modulation of one phase leg is taken as a case. It is observed that S_3 is switched in identical with S_5, but in complementary with S_1; and S_2 is switched in identical with S_6, but in complementary with S_4.
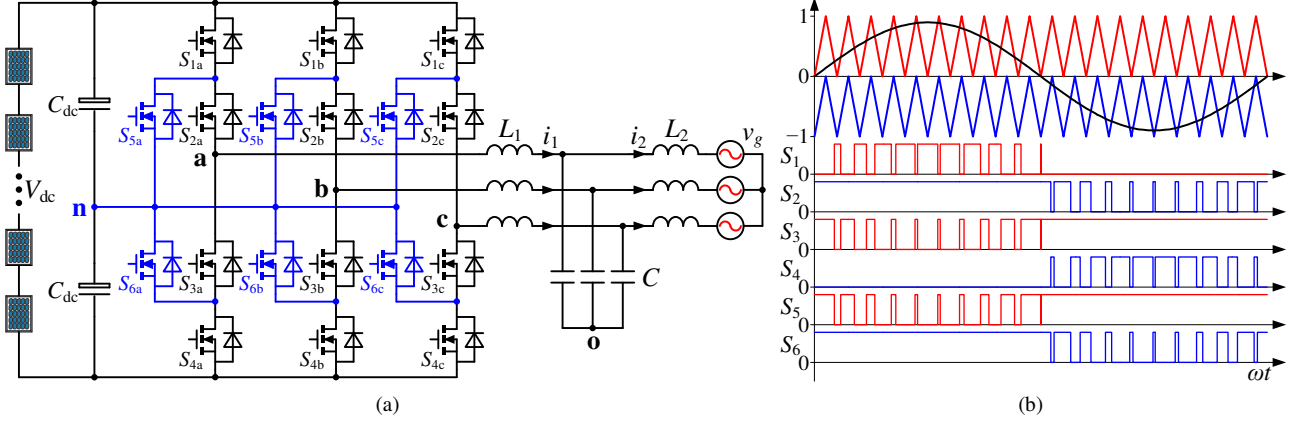
Fig. 1. Topology and modulation of a three-phase 3L-ANPC PV inverter with an *LCL* filter. (a) Circuit topology. (b) SPWM modulation.
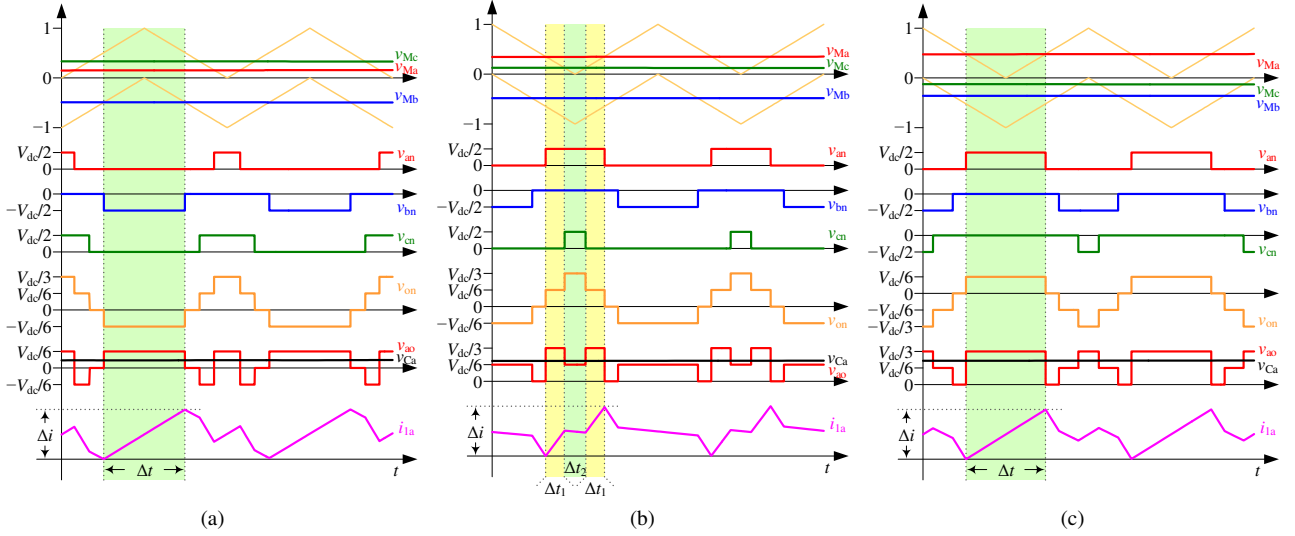

Fig. 2. Current ripple in L_1 for $0 < M_r \le \sqrt{3}/3$ at phase intervals (a) $\theta \in [0, \pi/6]$, (b) $\theta \in (\pi/6, \pi/3]$, and (c) $\theta \in (\pi/3, \pi/2]$.

III. INDUCTOR CURRENT RIPPLE DISTRIBUTION

In an *LCL* filter, the current ripple locates mainly on the inverter side, and its peak-to-peak value Δi can be predicted according to the volt-second product applied on L_1. As shown in Fig. 1(a), the voltage drop on L_1 is the difference between the inverter output voltage v_{ao} and the capacitor voltage v_{Ca}, which are expressed as

$$v_{ao} = v_{an} - \frac{v_{an} + v_{bn} + v_{cn}}{3} \qquad (1)$$

$$v_{Ca} = \frac{1}{2} M_r V_{dc} \sin \theta \qquad (2)$$

where M_r and θ are the modulation index and the phase angle, respectively. Since Δi is symmetric per quarter line cycle, only the first quarter ($0 \le \theta \le \pi/2$) is considered in this paper. v_{ao} is determined by the three-phase modulation references v_{Ma}, v_{Mb}, and v_{Mc}, which are expressed as

$$\begin{cases} v_{Ma} = M_r \sin \theta \\ v_{Mb} = M_r \sin\left(\theta - 2\pi/3\right) \\ v_{Mc} = M_r \sin\left(\theta + 2\pi/3\right) \end{cases} \qquad (3)$$

In a switching cycle, v_{Ca} is almost constant, thus Δi is dominated by v_{ao}, whose value changes frequently between multi levels ($0, \pm V_{dc}/6, \pm V_{dc}/3, \pm V_{dc}/2, \pm 2V_{dc}/3$) depending on M_r and θ. As a result, Δi is a function of M_r and θ. Specifically, M_r can be divided into three regions, which are $(0, \sqrt{3}/3]$, $(\sqrt{3}/3, 2/3]$, and $(2/3, 1]$. In each region, there are several intervals of θ, which are shown as follows.

A. $0 < M_r \le \sqrt{3}/3$

In this region, three phase intervals $[0, \pi/6)$, $(\pi/6, \pi/3]$, and $(\pi/3, \pi/2]$ exist, as shown in Fig. 2. Then, Δi can be readily identified in each phase interval, shown as the shaded areas in the figures. To calculate Δi, the time duration Δt (or Δt_1 and Δt_2) that each voltage level is applied on L_1 needs to be clarified at first.

If $\theta \in [0, \pi/6]$, shown as Fig. 2(a), Δt is related to v_{Mb} by

$$\Delta t = -v_{Mb} \cdot T_{sw} = -M_r \sin\left(\theta - 2\pi/3\right) \cdot T_{sw} \qquad (4)$$

where T_{sw} is the switching period. Then, Δi can be derived as

$$\Delta i = \left| \left(\frac{V_{dc}}{6} - v_{Ca} \right) \cdot \frac{\Delta t}{L_1} \right| = \frac{M_r V_{dc}}{2L_1 f_{sw}} \left| \sin\left(\theta - \frac{2\pi}{3}\right) \left(\frac{1}{3} - M_r \sin \theta \right) \right| \qquad (5)$$

where $f_{sw} = 1/T_{sw}$ is the switching frequency.

If $\theta \in (\pi/6, \pi/3]$, shown as Fig. 2(b), there are two time durations Δt_1 and Δt_2, where Δt_1 is calculated as

$$\Delta t_1 = \frac{1}{2}\left(v_{Ma} - v_{Mc}\right) \cdot T_{sw} = \frac{1}{2} M_r \left[\sin \theta - \sin\left(\theta + \frac{2\pi}{3}\right) \right] \cdot T_{sw} \qquad (6)$$
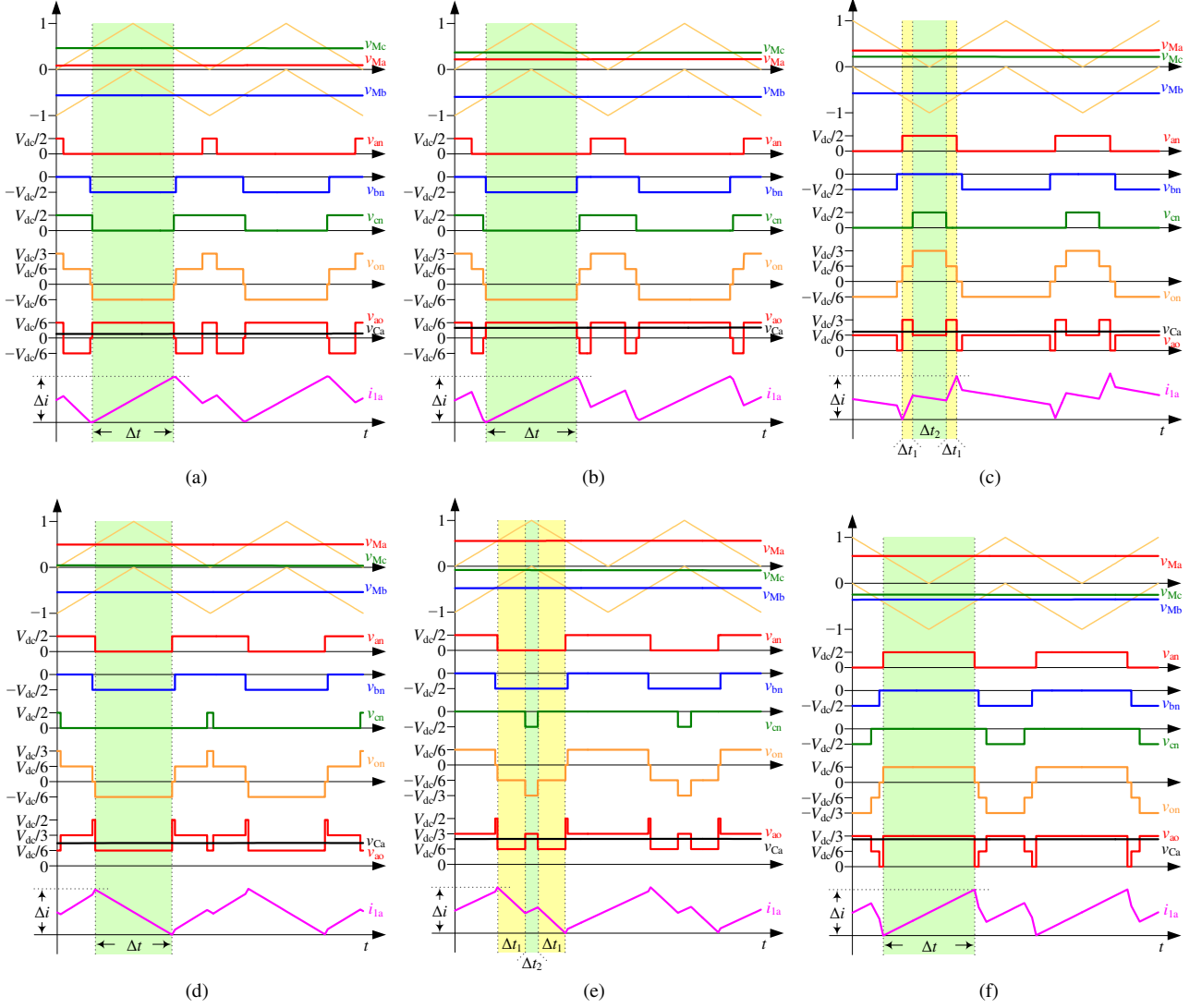
Fig. 3. Current ripple in L_1 for $\sqrt{3}/3 < M_r \le 2/3$. (a) $\theta \in [0, \theta_{B1}]$. (b) $\theta \in (\theta_{B1}, \pi/6]$. (c) $\theta \in (\pi/6, \theta_{B2}]$. (d) $\theta \in (\theta_{B2}, \pi/3]$. (e) $\theta \in (\pi/3, \theta_{B3}]$. (f) $\theta \in (\theta_{B3}, \pi/2]$.

Δt_2 is determined by v_{Mc} as

$$\Delta t_2 = v_{Mc} \cdot T_{sw} = M_r \sin(\theta + 2\pi/3) \cdot T_{sw} \qquad (7)$$

Then, Δi in this phase interval can be derived as

$$\Delta i = \left| \left(\frac{V_{dc}}{3} - v_{Ca} \right) \cdot \frac{2\Delta t_1}{L_1} + \left(\frac{V_{dc}}{6} - v_{Ca} \right) \cdot \frac{\Delta t_2}{L_1} \right|$$
$$= \frac{M_r V_{dc}}{2 L_1 f_{sw}} \left| \sin\theta + \frac{1}{3} \sin\left(\theta - \frac{2\pi}{3} \right) - M_r \sin^2 \theta \right| \qquad (8)$$

If $\theta \in (\pi/3, \pi/2)$, shown as Fig. 2(c), Δt is related to v_{Ma} by

$$\Delta t = v_{Ma} \cdot T_{sw} = M_r \sin\theta \cdot T_{sw} \qquad (9)$$

Then, Δi in this phase interval can be derived as

$$\Delta i = \left| \left(\frac{V_{dc}}{3} - v_{Ca} \right) \cdot \frac{\Delta t}{L_1} \right| = \frac{M_r V_{dc}}{2 L_1 f_{sw}} \left| \sin\theta \cdot \left(\frac{2}{3} - M_r \sin\theta \right) \right| \qquad (10)$$

B. $\sqrt{3}/3 < M_r \le 2/3$

In this region, six phase intervals $[0, \theta_{B1}]$, $(\theta_{B1}, \pi/6]$, $(\pi/6, \theta_{B2}]$, $(\theta_{B2}, \pi/3]$, $(\pi/3, \theta_{B3}]$, and $(\theta_{B3}, \pi/2]$ exist, as shown in Fig. 3. Except for $\pi/6$ and $\pi/3$, there are three additional phase boundaries, i.e., θ_{B1}, θ_{B2}, and θ_{B3}. θ_{B1} is obtained by assuming $v_{Mc} = 1 + v_{Mb}$, which gives rise to

$$\theta_{B1} = \arccos \frac{1}{\sqrt{3}M_r} \qquad (11)$$

θ_{B2} and θ_{B3} are obtained by assuming $v_{Ma} = 1 + v_{Mb}$ in phase intervals $[\pi/6, \pi/3]$ and $[\pi/3, \pi/2]$, which leads to

$$\begin{cases} \theta_{B2} = \arcsin 1/\left(\sqrt{3}M_r \right) - \pi/6 \\ \theta_{B3} = 5\pi/6 - \arcsin 1/\left(\sqrt{3}M_r \right) \end{cases} \qquad (12)$$

If $\theta \in [0, \theta_{B1}]$, shown as Fig. 3(a), Δt is related to v_{Mc} by

$$\Delta t = (1 - v_{Mc}) \cdot T_{sw} = \left[1 - M_r \sin(\theta + 2\pi/3) \right] \cdot T_{sw} \qquad (13)$$

Then, Δi in this phase interval can be derived as

$$\Delta i = \left| \left(\frac{V_{dc}}{6} - v_{Ca} \right) \cdot \frac{\Delta t}{L_1} \right|$$
$$= \frac{M_r V_{dc}}{2 L_1 f_{sw}} \left| \frac{1}{3M_r} + M_r \sin\theta \cdot \sin\left(\theta + \frac{2\pi}{3} \right) - \sin\theta - \frac{1}{3} \sin\left(\theta + \frac{2\pi}{3} \right) \right| \qquad (14)$$

If $\theta \in (\theta_{B1}, \pi/6)$, shown as Fig. 3(b), Δt is related to v_{Mb} by the same equation in (4), and then Δi is calculated as (5).

If $\theta \in (\pi/6, \theta_{B2})$, shown as Fig. 3(c), there are two time durations Δt_1 and Δt_2, which are the same as (6) and (7). Consequently, Δi can be calculated as (8).
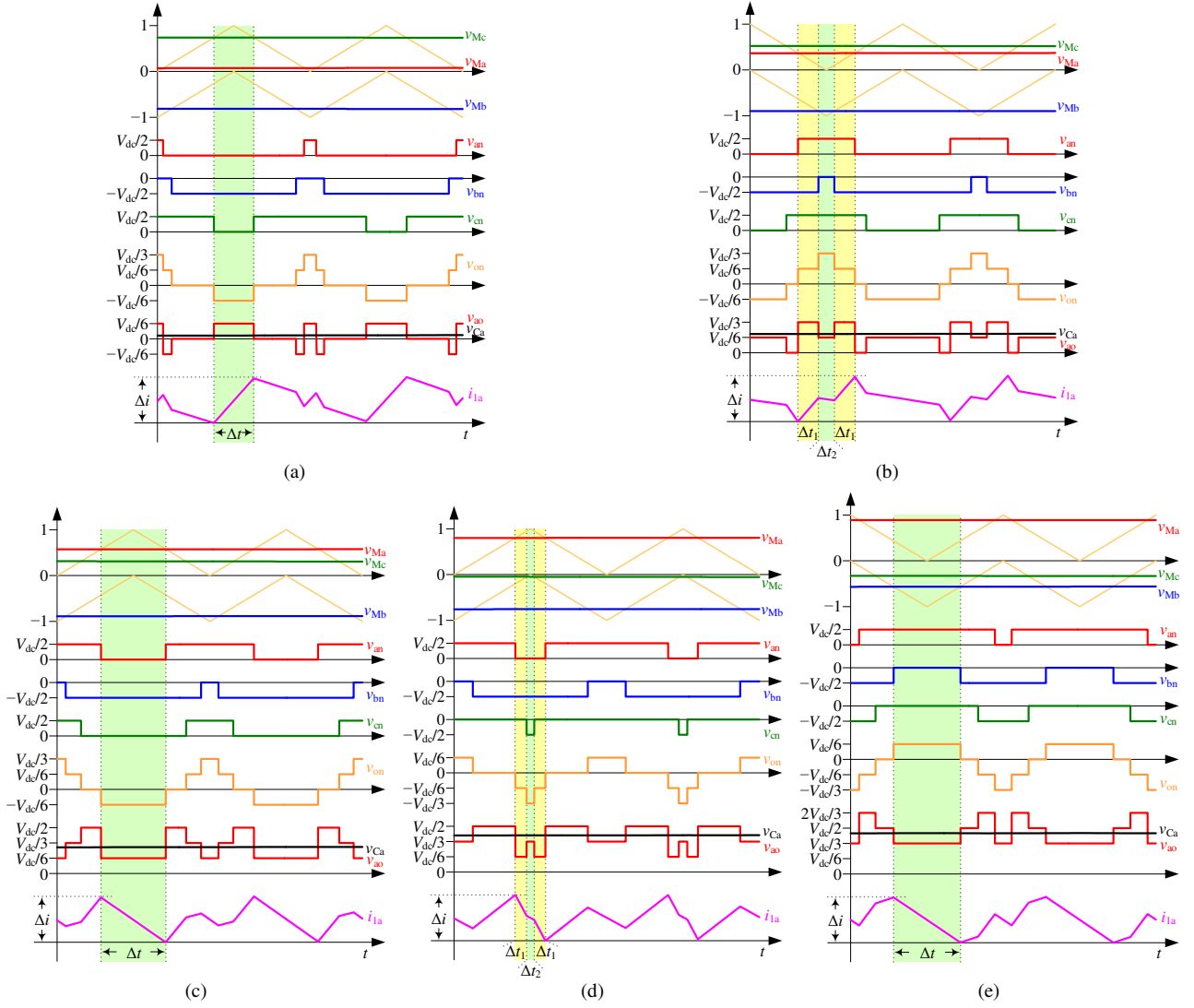
Fig. 4. Current ripple in L_1 for $2/3 < M_r \le 1$. (a) $\theta \in [0, \theta_{B2}]$. (b) $\theta \in (\theta_{B2}, \pi/6]$. (c) $\theta \in (\pi/6, \pi/3]$. (d) $\theta \in (\pi/3, \theta_{B4}]$. (e) $\theta \in (\theta_{B4}, \pi/2]$.

If $\theta \in (\theta_{B2}, \pi/3]$, shown as Fig. 3(d), Δt is related to v_{Ma} by

$$\Delta t = (1 - v_{Ma}) \cdot T_{sw} = (1 - M_r \sin\theta) \cdot T_{sw} \qquad (15)$$

Then, Δi in this phase interval can be derived as

$$\Delta i = \left| \left(\frac{V_{dc}}{6} - v_{Ca} \right) \cdot \frac{\Delta t}{L_1} \right| = \frac{M_r V_{dc}}{2L_1 f_{sw}} \left| \frac{1}{3M_r} + M_r \sin^2\theta - \frac{4}{3}\sin\theta \right| \qquad (16)$$

If $\theta \in (\pi/3, \theta_{B3}]$, shown as Fig. 3(e), there are two time durations Δt_1 and Δt_2, which are calculated as

$$\Delta t_1 = \frac{1}{2}(1 - v_{Ma} + v_{Mc}) \cdot T_{sw}$$
$$= \frac{1}{2}\left[1 - M_r \sin\theta + M_r \sin\left(\theta + \frac{2\pi}{3} \right) \right] \cdot T_{sw} \qquad (17)$$

$$\Delta t_2 = -v_{Mc} \cdot T_{sw} = -M_r \sin\left(\theta + 2\pi/3 \right) \cdot T_{sw} \qquad (18)$$

Then, Δi in this phase interval can be derived as

$$\Delta i = \left| \left(\frac{V_{dc}}{6} - v_{Ca} \right) \cdot \frac{2\Delta t_1}{L_1} + \left(\frac{V_{dc}}{3} - v_{Ca} \right) \cdot \frac{\Delta t_2}{L_1} \right|$$
$$= \frac{M_r V_{dc}}{2L_1 f_{sw}} \left| \frac{1}{3M_r} + M_r \sin^2\theta - \sin\theta + \frac{1}{3}\sin\left(\theta - \frac{2\pi}{3} \right) \right| \qquad (19)$$

If $\theta \in (\theta_{B3}, \pi/2]$, shown as Fig. 3(f), Δt is related to v_{Ma} by the same equation in (9), and then Δi is calculated as (10).

C. $2/3 < M_r \le 1$

In this region, there are five phase intervals $[0, \theta_{B2}]$, $(\theta_{B2}, \pi/6]$, $(\pi/6, \pi/3]$, $(\pi/3, \theta_{B4}]$, and $(\theta_{B4}, \pi/2]$. The extra phase boundary θ_{B4} is obtained by assuming $v_{Ma} = 1 + v_{Mc}$ in phase interval $[\pi/3, \pi/2]$, which gives rise to

$$\theta_{B4} = \arcsin\frac{1}{\sqrt{3}M_r} + \frac{\pi}{6} \qquad (20)$$

If $\theta \in [0, \theta_{B2}]$, shown as Fig. 4(a), Δt is related to v_{Mc} by the same equation in (13), and then Δi is calculated as (14).

If $\theta \in (\theta_{B2}, \pi/6]$, shown as Fig. 4(b), there are two time durations Δt_1 and Δt_2, where are calculated as

$$\Delta t_1 = \frac{1}{2}(v_{Ma} - v_{Mb} - 1) \cdot T_{sw}$$
$$= \frac{1}{2}\left[M_r \sin\theta - M_r \sin\left(\theta - \frac{2\pi}{3} \right) - 1 \right] \cdot T_{sw} \qquad (21)$$

$$\Delta t_2 = (1 + v_{Mb}) \cdot T_{sw} = \left[1 + M_r \sin\left(\theta - 2\pi/3 \right) \right] \cdot T_{sw} \qquad (22)$$

Then, Δi in this phase interval can be derived as

M_r	θ	Normalized current ripple $\Delta\lambda$
(0, $\sqrt{3}$ /3]	[0, π/6] @ Fig. 2(a)	$\Delta\lambda_{A1} = |\sin(\theta - 2\pi/3)(1/3 - M_r\sin\theta)|$
	(π/6, π/3] @ Fig. 2(b)	$\Delta\lambda_{A2} = |\sin\theta + 1/3\cdot\sin(\theta - 2\pi/3) - M_r\sin^2\theta|$
	(π/3, π/2] @ Fig. 2(c)	$\Delta\lambda_{A3} = |\sin\theta\cdot(2/3 - M_r\sin\theta)|$
($\sqrt{3}$ /3, 2/3]	[0, θ_{B1}] @ Fig. 3(a)	$\Delta\lambda_{B1} = |1/(3M_r) + M_r\sin\theta\cdot\sin(\theta + 2\pi/3) - \sin\theta - 1/3\cdot\sin(\theta + 2\pi/3)|$
	(θ_{B1}, π/6] @ Fig. 3(b)	$\Delta\lambda_{B2} = |\sin(\theta - 2\pi/3)(1/3 - M_r\sin\theta)|$
	(π/6, θ_{B2}] @ Fig. 3(c)	$\Delta\lambda_{B3} = |\sin\theta + 1/3\cdot\sin(\theta - 2\pi/3)\cdot - M_r\sin^2\theta|$
	(θ_{B2}, π/3] @ Fig. 3(d)	$\Delta\lambda_{B4} = |1/(3M_r) + M_r\sin^2\theta - 4/3\cdot\sin\theta|$
	(π/3, θ_{B3}] @ Fig. 3(e)	$\Delta\lambda_{B5} = |1/(3M_r) + M_r\sin^2\theta - \sin\theta + 1/3\cdot\sin(\theta - 2\pi/3)|$
	(θ_{B3}, π/2] @ Fig. 3(f)	$\Delta\lambda_{B6} = |\sin\theta\cdot(2/3 - M_r\sin\theta)|$
(2/3, 1]	[0, θ_{B2}] @ Fig. 4(a)	$\Delta\lambda_{C1} = |1/(3M_r) + M_r\sin\theta\cdot\sin(\theta + 2\pi/3) - \sin\theta - 1/3\cdot\sin(\theta + 2\pi/3)|$
	(θ_{B2}, π/6] @ Fig. 4(b)	$\Delta\lambda_{C2} = |1/(3M_r) + M_r\sin^2\theta - \sin\theta - 1/3\cdot\sin(\theta + 2\pi/3)|$
	(π/6, π/3] @ Fig. 4(c)	$\Delta\lambda_{C3} = |1/(3M_r) + M_r\sin^2\theta - 4/3\cdot\sin\theta|$
	(π/3, θ_{B4}] @ Fig. 4(d)	$\Delta\lambda_{C4} = |1/(3M_r) + M_r\sin^2\theta - \sin\theta + 1/3\cdot\sin(\theta - 2\pi/3)|$
	(θ_{B4}, π/2] @ Fig. 4(e)	$\Delta\lambda_{C5} = |2/(3M_r) - M_r\sin\theta\cdot\sin(\theta - 2\pi/3) - \sin\theta + 2/3\cdot\sin(\theta - 2\pi/3)|$

$$\Delta i = \left| \left(\frac{V_{dc}}{3} - v_{Ca}\right)\cdot\frac{2\Delta t_1}{L_1} + \left(\frac{V_{dc}}{6} - v_{Ca}\right)\cdot\frac{\Delta t_2}{L_1} \right|$$

$$= \frac{M_r V_{dc}}{2L_1 f_{sw}} \left| \frac{1}{3M_r} + M_r\sin^2\theta - \sin\theta - \frac{1}{3}\sin\left(\theta + \frac{2\pi}{3}\right) \right| \tag{23}$$

If $\theta \in (\pi/6, \pi/3]$, shown as Fig. 4(c), Δt is related to v_{Ma} by the same equation in (15), and then Δi is calculated as (16).

If $\theta \in (\pi/3, \theta_{B4}]$, shown as Fig. 4(d), there are two time durations Δt_1 and Δt_2, which are the same as (17) and (18). Consequently, Δi can be calculated as (19).

If $\theta \in (\theta_{B4}, \pi/2]$, shown as Fig. 4(e), Δt is related to v_{Mb} by

$$\Delta t = (1 + v_{Mb})\cdot T_{sw} = \left[1 + M_r\sin(\theta - 2\pi/3)\right]\cdot T_{sw} \tag{24}$$

Then, Δi in this phase interval can be derived as

$$\Delta i = \left| \left(\frac{V_{dc}}{3} - v_{Ca}\right)\cdot\frac{\Delta t}{L_1} \right|$$

$$= \frac{M_r V_{dc}}{2L_1 f_{sw}} \left| \frac{2}{3M_r} - M_r\sin\theta\cdot\sin\left(\theta - \frac{2\pi}{3}\right) - \sin\theta + \frac{2}{3}\sin\left(\theta - \frac{2\pi}{3}\right) \right| \tag{25}$$

To demonstrate the general features of the inductor current ripple, Δi can be normalized by $\Delta\lambda$ as

$$\Delta i = \frac{M_r V_{dc}}{2L_1 f_{sw}}\cdot\Delta\lambda = \sqrt{\frac{2}{3}}\frac{V_{g(LL)}}{L_1 f_{sw}}\cdot\Delta\lambda \tag{26}$$

where $V_{g(LL)}$ is the grid voltage RMS value (line to line). Based on this, $\Delta\lambda$ can be obtained for all the phase intervals in the entire modulation range, as shown in Table I.

IV. ANALYSIS OF CURRENT RIPPLE CHARACTERISTICS

Based on the results in Table I, the current ripple distribution in a quarter line cycle is shown in Fig. 5, where three M_r values (M_r = 0.5, 0.6, and 0.9) that locate in the different regions are taken as instances. From this figure, the maximum current ripple $\Delta\lambda_{max}$ can be clearly identified. For example, under M_r = 0.5 and 0.6, $\Delta\lambda_{max}$ occurs at the zero crossing instant (i.e., θ = 0); under M_r = 0.9, $\Delta\lambda_{max}$ occurs at the peak voltage instant (i.e., $\theta = \pi/2$). Actually, except for these two instants, $\Delta\lambda_{max}$ may occur at other phase angles depending on M_r.

If $0 < M_r \le \sqrt{3}$ /3, $\Delta\lambda_{max}$ can occur at either θ = 0 or $\theta = \pi/2$. From Table I, $\Delta\lambda$ at these two instants are obtained as

$$\Delta\lambda = \begin{cases} \dfrac{\sqrt{3}}{6}, & \theta = 0 \\ \dfrac{2}{3} - M_r, & \theta = \dfrac{\pi}{2} \end{cases} \tag{27}$$

Assuming $2/3 - M_r = \sqrt{3}$ /6, the boundary value of M_r is calculated as $M_r = 2/3 - \sqrt{3}$ /6.

If $\sqrt{3}$ /3 $< M_r \le$ 2/3, $\Delta\lambda_{max}$ definitely occurs at θ = 0 with

$$\Delta\lambda = \frac{1}{3M_r} - \frac{\sqrt{3}}{6} \tag{28}$$

If 2/3 $< M_r \le$ 1, $\Delta\lambda_{max}$ can occur at θ = 0, $\theta = \pi/2$, or a certain value in the interval (π/6, π/3]. From Table I, $\Delta\lambda$ at θ = 0 and $\theta = \pi/2$ can be obtained as

$$\Delta\lambda = \begin{cases} \dfrac{1}{3M_r} - \dfrac{\sqrt{3}}{6}, & \theta = 0 \\ \dfrac{4}{3} - \dfrac{2}{3M_r} - \dfrac{M_r}{2}, & \theta = \dfrac{\pi}{2} \end{cases} \tag{29}$$

$\Delta\lambda_{max}$ in the phase interval (π/6, π/3] can be derived by assuming $\Delta\lambda_{C3}' = 0$ in Table I, which gives rise to

$$\sin\theta = \frac{2}{3M_r} \tag{30}$$

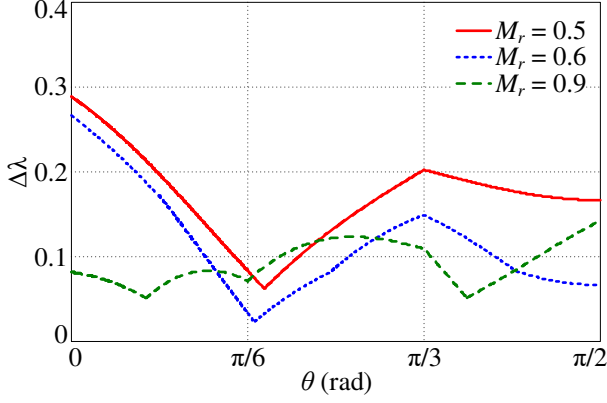Substituting (30) into $\Delta\lambda_{C3}$, $\Delta\lambda_{max}$ in (π/6, π/3] is derived as

Fig. 5. Inductor current ripple distribution for different M_r.

Fig. 6. Curves of $\Delta\lambda_{\max}$ and $\Delta\lambda_{AV}$ as a function of M_r.

$$\Delta\lambda_{\max} = \frac{1}{9M_r} \tag{31}$$

Letting (29) equal to (31), two boundary values of M_r are calculated as $M_r = 4/(3\sqrt{3})$ and $M_r = 4/3 - \sqrt{2}/3$.

Combining (27)~(29) and (31), and considering the four boundary values of M_r, $\Delta\lambda_{\max}$ in the entire modulation range can be obtained as

$$\Delta\lambda_{\max} = \begin{cases} \dfrac{2}{3} - M_r, & 0 < M_r \le \dfrac{2}{3} - \dfrac{\sqrt{3}}{6} \\[2mm] \dfrac{\sqrt{3}}{6}, & \dfrac{2}{3} - \dfrac{\sqrt{3}}{6} < M_r \le \dfrac{\sqrt{3}}{3} \\[2mm] \dfrac{1}{3M_r} - \dfrac{\sqrt{3}}{6}, & \dfrac{\sqrt{3}}{3} < M_r \le \dfrac{4}{3\sqrt{3}} \\[2mm] \dfrac{1}{9M_r}, & \dfrac{4}{3\sqrt{3}} < M_r \le \dfrac{4}{3} - \dfrac{\sqrt{2}}{3} \\[2mm] \dfrac{4}{3} - \dfrac{2}{3M_r} - \dfrac{M_r}{2}, & \dfrac{4}{3} - \dfrac{\sqrt{2}}{3} < M_r \le 1 \end{cases} \tag{32}$$

Recalling Fig. 5, it can be found that the instantaneous current ripple varies significantly with the phase angle. $\Delta\lambda_{\max}$ at a single phase angle is thus inadequate to quantify the overall ripple level. For this reason, the concept of average current ripple $\Delta\lambda_{AV}$ is introduced here. Referring to Table I, $\Delta\lambda_{AV}$ in the three different regions can be expressed as (33), shown at the bottom of this page.

According to (32) and (33), the curves of $\Delta\lambda_{\max}$ and $\Delta\lambda_{AV}$ as a function of M_r are shown in Fig. 6. With the increase of M_r, $\Delta\lambda_{\max}$ first decreases and then increases with a minimum value at $M_r = 0.86$, and $\Delta\lambda_{AV}$ first decreases and then stays almost constant with a corner point at $M_r = 0.7$. Thus, $M_r = 0.86$ is an optimal operating point where the ripple level is minimized. This can be designed as the nominal operation condition of the 3L-ANPC PV inverter, as shown by a case study in the next section.

TABLE II
SYSTEM PARAMETERS IN CASE STUDY

Parameter	Symbol	Value	Parameter	Symbol	Value
DC voltage (nominal)	V_{dc}	1140 V	Inverter-side inductor	L_1	250 μH
Grid voltage (RMS)	$V_{g(LL)}$	600 V	Grid-side inductor	L_2	40 μH
Output power	P_0	12 kW	Filter capacitor	C	5 μF
Fundamental frequency	f_0	50 Hz	Switching frequency	f_{sw}	48 kHz

V. CASE STUDY

To verify the theoretical analysis, a case study is presented in this section. The system parameters are listed in Table II. For the PV inverter, the maximum DC input voltage is 1500 V, and there is a DC voltage operating range around a nominal value [1]. The selection of this nominal value is critical to achieve a high efficiency. Here, the nominal DC voltage is designed for a target $M_r = 0.86$, which corresponds to $V_{dc} = 1140$ V.

The *LCL* filter is designed with well-known constraints [13], [20]. Specifically, $L_1 = 250\ \mu$H is obtained for an average current ripple of 23% of the rated peak current, $C = 5\ \mu$F is designed to limit the reactive power to 5% of the rated output power, and $L_2 = 40\ \mu$H is set to attenuate the switching harmonics to 0.3% of the rated peak current.

$M_r = 0.5$, 0.6, and 0.9 are verified here, and their simulation results are given in Fig. 7, where the upper part shows the entire inverter-side inductor current i_1 and the lower part shows the extracted ripple current Δi. Δi is obtained by subtracting the average current value (i.e., the fundamental current) from i_1. It can be seen that the calculated ripple value exactly covers the envelope of the extracted ripple current, which implies a close match of the theoretical analysis and the simulation result.

$$\Delta\lambda_{AV} = \begin{cases} \dfrac{2}{\pi}\left(\int_0^{\frac{\pi}{6}} \Delta\lambda_{A1}d\theta + \int_{\frac{\pi}{6}}^{\frac{\pi}{3}} \Delta\lambda_{A2}d\theta + \int_{\frac{\pi}{3}}^{\frac{\pi}{2}} \Delta\lambda_{A3}d\theta \right), & 0 < M_r \le \dfrac{\sqrt{3}}{3} \\[3mm] \dfrac{2}{\pi}\left(\int_0^{\theta_{B1}} \Delta\lambda_{B1}d\theta + \int_{\theta_{B1}}^{\frac{\pi}{6}} \Delta\lambda_{B2}d\theta + \int_{\frac{\pi}{6}}^{\theta_{B2}} \Delta\lambda_{B3}d\theta + \int_{\theta_{B2}}^{\frac{\pi}{3}} \Delta\lambda_{B4}d\theta + \int_{\frac{\pi}{3}}^{\theta_{B3}} \Delta\lambda_{B5}d\theta + \int_{\theta_{B3}}^{\frac{\pi}{2}} \Delta\lambda_{B6}d\theta \right), & \dfrac{\sqrt{3}}{3} < M_r \le \dfrac{2}{3} \\[3mm] \dfrac{2}{\pi}\left(\int_0^{\theta_{B2}} \Delta\lambda_{C1}d\theta + \int_{\theta_{B2}}^{\frac{\pi}{6}} \Delta\lambda_{C2}d\theta + \int_{\frac{\pi}{6}}^{\frac{\pi}{3}} \Delta\lambda_{C3}d\theta + \int_{\frac{\pi}{3}}^{\theta_{B4}} \Delta\lambda_{C4}d\theta + \int_{\theta_{B4}}^{\frac{\pi}{2}} \Delta\lambda_{C5}d\theta \right), & \dfrac{2}{3} < M_r \le 1 \end{cases} \tag{33}$$
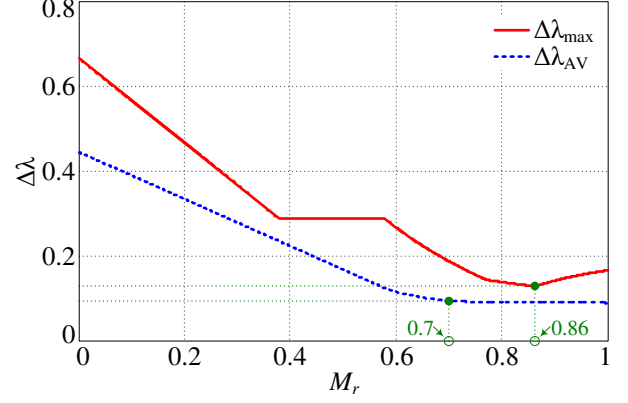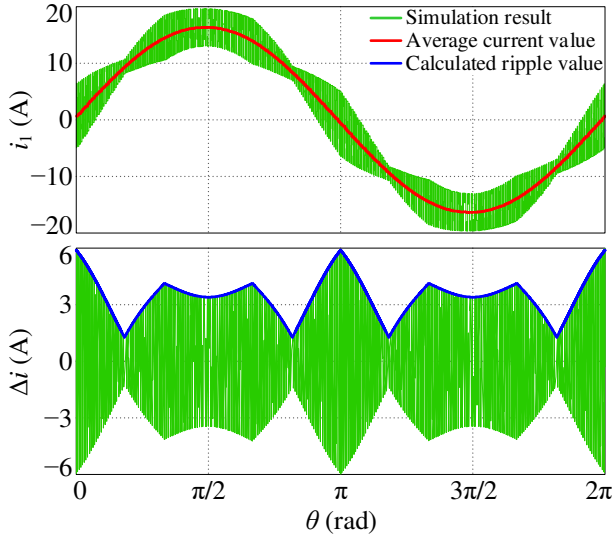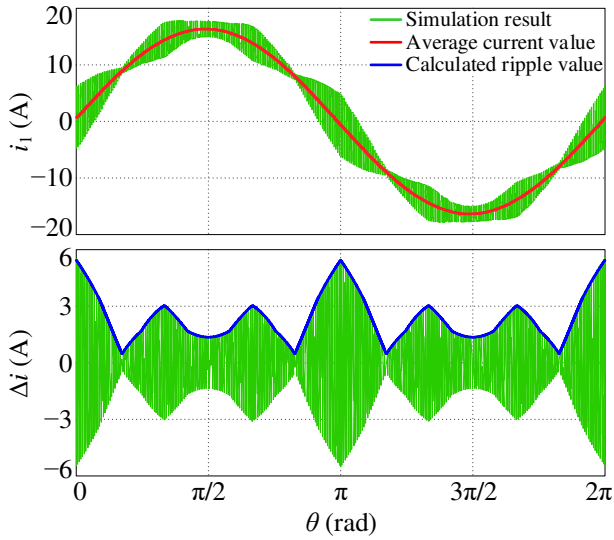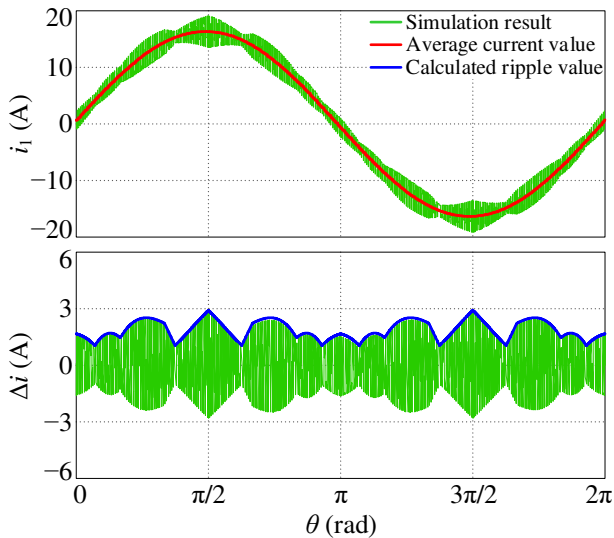
Fig. 7. Simulation results with different M_r. (a) $M_r = 0.5$. (b) $M_r = 0.6$. (c) $M_r = 0.9$.

VI. CONCLUSIONS

Precise inductor current ripple distribution of a 3L-ANPC PV inverter has been derived in this paper. For the entire modulation range, the maximum current ripple is readily identified, and the concept of average current ripple is proposed to quantify the overall ripple level. A minimum ripple level is found at the modulation index of 0.86, and it is designed as the system nominal operation condition by setting the DC voltage. The ripple analysis is carried out with SPWM modulation and can easily be extended to the SVM schemes. Simulation results from a case study verify the theoretical analysis.

REFERENCES

[1] E. Serban, M. Ordonez, and C. Pondiche, "DC-bus voltage range extension in 1500 V photovoltaic inverters," *IEEE J. Emerg. Sel. Topics Power Electron.*, vol. 3, no. 4, pp. 901−917, Dec. 2015.

[2] Z. Čorba, B. Popadić, V. Katić, B. Dumnić, and D. Milićević, "Future of high power PV plants — 1500 V inverters," in *Proc. 19th International Symposium on Power Electronics (Ee)*, Novi Sad, Serbia, Oct. 2017.

[3] *True 1500 V Technology for the New Gneration of PV Power Plants*, SMA Solar Technology AG. [Online]. Available: https://www.sma.de/fileadmin/content/global/specials/1500V/Whitepap1500V-AEN1639.pdf

[4] E. Gkoutioudi, P. Bakas, and A. Marinopoulos, "Comparison of PV systems with maximum DC voltage 1000 V and 1500 V," in *Proc. IEEE 39th Photovoltaic Specialists Conference (PVSC)*, Jun. 2013, pp. 2873−2878.

[5] R. Inzunza, R. Okuyama, T. Tanaka, and M. Kinoshita, "Development of a 1500 Vdc photovoltaic inverter for utility-scale PV power plants," in *Proc. IEEE 2nd International Future Energy Electronics Conference (IFEEC)*, Taipei, Taiwan, Nov. 2015.

[6] X. Hao, K.-W. Ma, Y. Yang, and J. Zhao, "1500 V solar inverter at megawatts level in NPC1 topology enabled by high-density IGBT module," in *Proc. IEEE Region 10 Conference (TENCON)*, Nov. 2016, pp. 2323−2326.

[7] A. Nabae, I. Takahashi, and H. Akagi, "A new neutral-point-clamped PWM inverter," *IEEE Trans. Ind. Appl.*, vol. 17, no. 5, pp. 518−523, Sep./Oct. 1981.

[8] T. Brückner, S. Bernet, and H. Güldner, "The active NPC converter and its loss-balancing control," *IEEE Trans. Ind. Electron.*, vol. 52, no. 3, pp. 855−868, Jun. 2005.

[9] J. Rodriguez, S. Bernet, P. K. Steimer, and I. E. Lizama, "A survey on neutral-point-clamped inverters," *IEEE Trans. Ind. Electron.*, vol. 57, no. 7, pp. 2219−2230, Jul. 2010.

[10] M. Chen, H. Wang, F. Blaabjerg, X. Wang, and D. Pan, "A temperature-dependent thermal model of silicon carbide MOSFET module for long-term reliability assessment," in *Proc. IEEE 4th Southern Power Electronics Conference (SPEC)*, Singapore, Dec. 2018.

[11] M. Chen, H. Wang, H. Wang, F. Blaabjerg, X. Wang, and D. Pan, "Reliability assessment of hybrid capacitor bank using electrolytic- and film-capacitors in three-level neutral-point-clamped inverters," in *Proc. IEEE Applied Power Electronics Conference and Exposition (APEC)*, Mar. 2019, pp. 2826−2832.

[12] Y. Jiao and F. C. Lee, "*LCL* filter design and inductor current ripple analysis for a three-level NPC grid interface converter," *IEEE Trans. Power Electron.*, vol. 30, no. 9, pp. 4659−4668, Sep. 2015.

[13] D. Pan, X. Ruan, X. Wang, F. Blaabjerg, X. Wang, and Q. Zhou, "A highly robust single-loop current control scheme

for grid-connected inverter with an improved *LCCL* filter configuration," *IEEE Trans. Power Electron.*, vol. 33, no. 10, pp. 8474−8487, Oct. 2018.

[14] A. Kouchaki and M. Nymand, "Analytical design of passive *LCL* filter for three-phase two-level power factor correction rectifiers," *IEEE Trans. Power Electron.*, vol. 33, no. 4, pp. 3012−3022, Apr. 2018.

[15] D. Jiang and F. Wang, "Variable switching frequency PWM for three-phase converters based on current ripple prediction," *IEEE Trans. Power Electron.*, vol. 28, no. 11, pp. 4951−4961, Nov. 2013.

[16] D. Jiang and F. Wang, "Current-ripple prediction for three-phase PWM converters," *IEEE Trans. Ind. Appl.*, vol. 50, no. 1, pp. 531−538, Jan./Feb. 2014.

[17] X. Ruan, X. Wang, D. Pan, D. Yang, W. Li, and C. Bao, *Control Techniques for LCL-Type Grid-Connected Inverters.* Singapore: Springer, 2018.

[18] G. Grandi, J. Loncarski, and O. Dordevic, "Analytical evaluation of output current ripple amplitude in three-phase three-level inverters," *IET Power Electron.*, vol. 7, no. 9, pp. 2258−2268, Sep. 2014.

[19] G. Grandi, J. Loncarski, and O. Dordevic, "Analysis and comparison of peak-to-peak current ripple in two-level and multilevel PWM inverters," *IEEE Trans. Ind. Electron.*, vol. 62, no. 5, pp. 2721−2730, May 2015.

[20] D. Pan, X. Ruan, C. Bao, W. Li, and X. Wang, "Magnetic integration of the *LCL* filter in grid-connected inverters,"

IEEE Trans. Power Electron., vol. 29, no. 4, pp. 1573−1578, Apr. 2014.

[21] D. Pan, X. Ruan, C. Bao, W. Li, and X. Wang, "Capacitor-current-feedback active damping with reduced computation delay for improving robustness of *LCL*-type grid-connected inverter," *IEEE Trans. Power Electron.*, vol. 29, no. 7, pp. 3414−3427, Jul. 2014.

[22] D. Pan, X. Ruan, C. Bao, W. Li, and X. Wang, "Optimized controller design for *LCL*-type grid-connected inverter to achieve high robustness against grid-impedance variation," *IEEE Trans. Ind. Electron.*, vol. 62, no. 3, pp. 1537−1547, Mar. 2015.

[23] D. Pan, X. Ruan, X. Wang, H. Yu, and Z. Xing, "Analysis and design of current control schemes for *LCL*-type grid-connected inverter based on a general mathematical model," *IEEE Trans. Power Electron.*, vol. 32, no. 6, pp. 4395−4410, Jun. 2017.

[24] D. Pan, X. Ruan, and X. Wang, "Direct realization of digital differentiators in discrete domain for active damping of *LCL*-type grid-connected inverter," *IEEE Trans. Power Electron.*, vol. 33, no. 10, pp. 8461−8473, Oct. 2018.

[25] D. Barater, C. Concari, G. Buticchi, E. Gurpinar, D. De, and A. Castellazzi, "Performance evaluation of a three-level ANPC photovoltaic grid-connected inverter with 650-V SiC devices and optimized PWM," *IEEE Trans. Ind. Appl.*, vol. 52, no. 3, pp. 2475−2485, May/Jun. 2016.